AIAA JOURNAL
Vol. 44, No. 5, May 2006

Boundary-Layer Transition on an Axisymmetric Body at Incidence at Mach 1.2

Hiroki Sugiura,* Naoko Tokugawa,† and Yoshine Ueda‡
Japan Aerospace Exploration Agency, Tokyo 182-8522, Japan

Experimental investigation of the boundary-layer transition on an axisymmetric nose model at 1- and 2-deg incidence was conducted at Mach 1.2. The configuration of the model is the forward part of a Sears–Haack body defined to have minimum wave drag caused by volume at 0-deg incidence in supersonic flow. Transition locations were obtained with small surface roughness on the order of 0.1 μ using an infrared camera. An unsteady pressure transducer was applied to investigate instability mechanisms that lead to transition. These results show that the most aft transition occurred on the leeward ray rather than on the windward rays as observed on sharp cones. Tollmien–Schlichting instability dominated the transition process on the windward ray, and crossflow instability was assumed to dominate on the side similar to the transition on the sharp cones. However, transition occurred more aft on the leeward ray than for the case of the sharp cones, and the transition front was determined by turbulent wedges formed as a consequence of the more forward transition on the side. The disturbance believed to be a traveling crossflow wave was observed at 1-deg incidence, and its measured frequency was in good agreement with the maximum amplified frequency, which was calculated using a compressible linear e^N code.

Nomenclature

C_P	=	pressure coefficient
M	=	Mach number
P	=	pressure
P'	=	pressure fluctuation
P_0	=	total pressure
p	=	static pressure
Re	=	Reynolds number
s	=	distance along streamline
T	=	temperature
Tu	=	freestream turbulence
u	=	streamwise component of flow velocity
v	=	spanwise component of flow velocity
w	=	vertical component of flow velocity
x	=	distance measured axially from cone apex
α	=	angle of attack, deg
γ	=	intermittency factor
θ	=	meridian angle measured from leeward ray
ρ	=	density of air
ϕ	=	cone meridian angle measured from the intersection line of the model surface and the plane defined by the center axis of the model and the focal point of the camera

Subscripts

rms	=	root-mean-square average
unit	=	unit
0	=	freestream stagnation condition

Introduction

FRICTION drag makes up more than one-third of the drag of next-generation supersonic transports (SST), and its reduction by delaying boundary-layer transition remains an attractive and effective measure for improving the lift-to-drag ratio. Achievement of laminar flow for up to 60% of wing chord for a next-generation SST configuration has been estimated to produce a total-aircraft drag reduction of 14% (Ref. 1).

The flowfield over aircraft is, however, generally fully three-dimensional, and an understanding of three-dimensional boundary-layer transition is critical for delaying the transition. Although many issues remain unsettled in incompressible three-dimensional boundary layers, the present investigation is part of a project that begins serious study of transition mechanisms in supersonic three-dimensional boundary layers, which are the more relevant to supersonic flight.

The simplest geometries that exhibit three-dimensional supersonic boundary layers are round cones at angle of attack (AOA) and elliptic cones.[2] Round cones are useful in that two-dimensional flow is realized at zero AOA and varying the AOA can easily control three dimensionality.

Thus, a number of experiments have been conducted to investigate the transition for round cones at incidence.[3–6] The previous studies have consistently found that as the AOA is increased transition moves rearward on the windward ray and forward on the leeward side.[3–6] Stability experiments[7,8] showed that Tollmien–Schlichting (T-S) instability dominates the transition process on the windward ray. Observations of streamwise vortices[3,9,10] revealed that crossflow (C-F) instability dominates on the side. Boundary-layer-profile measurements[7,8] showed that flow profiles along the leeward ray are highly inflectional.

There are pressure gradients along streamlines at nonzero AOA (Fig. 1a), but no pressure gradient exists on sharp cones at zero AOA. However, large pressure gradients generally exist along streamlines on noses and wings of aircraft at zero AOA, and the gradients are much greater at nonzero AOA. Thus the question remains: "What occurs with large pressure gradients along streamlines, such as in noses and wings of aircraft?" All of the previous studies of transition on axisymmetric bodies at incidence[11,12] are restricted to subsonic speed except for those on cones.

It is unknown whether inflectional profile on the leeward ray exists in the presence of a large pressure gradient. Because favorable pressure gradients along the inviscid streamlines stabilize T-S instabilities and amplify C-F instabilities on the side, the transition front moves rearward on the windward ray and can move forward on the side. The difference in transition location can become sufficiently large so that the transition on the windward ray might be affected by the early transition on the side.

Presented as Paper 2004-0251 at the AIAA 42nd Aerospace Sciences Meeting, Reno, NV, 5–9 January 2004; received 2 March 2004; revision received 25 July 2005; accepted for publication 27 July 2005.

*Researcher, Aerodynamics Research Group, Chofu. Senior Member AIAA.
†Associate Senior Researcher, Aerodynamics Research Group, Chofu.
‡Researcher, Information Technology Center, Chofu.

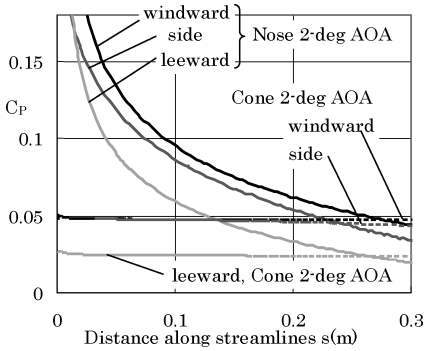

Fig. 1a Comparison of pressure distributions of the model with those of 10-deg cone.

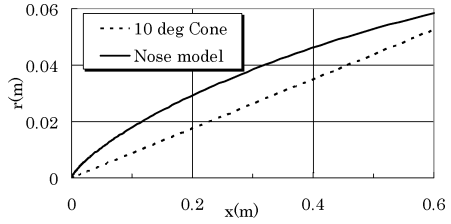

Fig. 1b Comparison of the model configuration with the 10-deg cone.

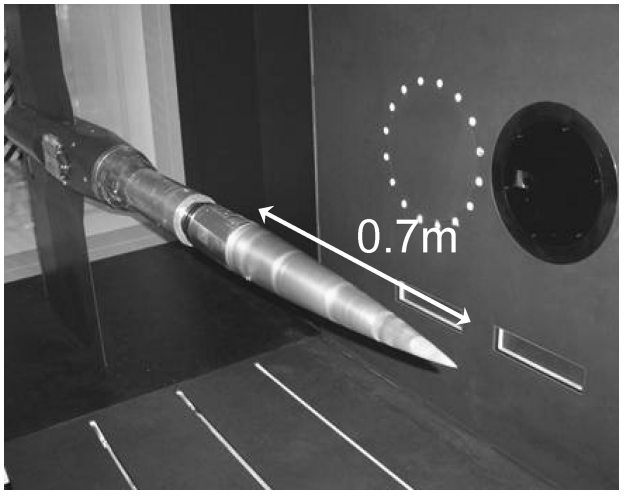

Fig. 2 Axisymmetric nose model.

The surface painted with an oil film, temperature-sensitive paints, liquid crystals, etc., is not suitable for studying the crossflow-induced transition, which is influenced by submicron surface roughness.[13] The present study uses an infrared (IR) camera to acquire the transition front with little influence of surface roughness.

The purposes of this paper are to 1) compare the three-dimensional boundary-layer transition with relatively small and large pressure gradients along streamlines and 2) investigate the underlying stability mechanisms determining transition location.

Experimental Procedure

Test Model

An axisymmetric nose model that is 700 mm long measured axially from apex to base was used (Fig. 2). The model is a 23.4% scale model of the nose of a nonpowered experimental supersonic transport airplane (NEXST-1) that was developed at Japan Aerospace Exploration Agency (JAXA). The configuration of the nose is the forward part of a Sears–Haack body defined to have minimum wave drag caused by volume at zero AOA (Fig. 1b) and is described by the following expression:

$$r = A(x/l)(1 - x/l)^{\frac{3}{4}} \tag{1}$$

When x and r are expressed in meters, $A = 217.59$, and $l = 2.692308$. The Sears–Haack body serves as a guideline reference for designing fuselages of supersonic aircraft.

The model is made of insulated material so that surface-temperature distribution can be acquired by an IR camera. The IR camera technique usually requires the use of adiabatic material to maintain the differences in wall temperature.

Use of resin with high processability allows us to attain the transition front with little influence of surface roughness. Thus, the model is made of an amorphous fiber-reinforced plastic called polysulfone. The rms amplitude of the roughness of the model is 0.22 μm. No bluntness effect exists on the model because its geometry is defined to be blunt.

An unsteady pressure transducer is installed at $x = 620$ mm location on the model, and static-pressure fluctuation can be measured on the surface. By varying the roll angle of the model, circumferential distribution of the fluctuation can be obtained. The pressure transducer is 1.6 mm in diameter and is mounted flush with the model surface. No level difference was identified through examination by touch and was confirmed with a thickness gauge to be below 50 μm.

For static-pressure measurements, another model with the same configuration was used. The model had six static ports.

Test Facility

The experiment was conducted in the 2×2 m transonic wind tunnel of JAXA in Japan.

The static-pressure fluctuation normalized by dynamic pressure $C_{P\text{rms}}$ at $M = 1.2$ was 0.34% in the tunnel, which was measured with bandwidth from 25 Hz to 20 kHz (Ref. 14). The tunnel was the available transonic tunnel with the lowest turbulence level. However, without such care as taken in the quiet tunnels, the tunnel-wall boundary layer is apparently turbulent. Figure 3 shows the power spectrum of the static-pressure fluctuation on a 10-deg cone at $M = 1.2$ measured by Oguni et al.[14] There is no particular frequency dependency in the fluctuation. Figure 4b shows the power spectrum of the static-pressure fluctuation of a laminar boundary layer on the present model at 0-deg AOA and $M = 1.2$ measured with bandwidth from 125 Hz to 100 kHz. This power spectrum shows that the pressure fluctuation is at a lower level above 20 kHz than below 20 kHz.

Figures 4a and 4b show the effect of total pressure on the surface-pressure fluctuation on the present model and its spectral content, respectively, at 0-deg AOA and $M = 1.2$. It is clear that the total pressure has little effect on the pressure fluctuation and its spectral content. Varying the total pressure can control unit Reynolds-number so that by varying the total pressure of the tunnel from 50 to 70 kPa the unit Reynolds-number effect on the transition can be studied.

Flow conditions examined in the present experiment are summarized in Table 1. Flow conditions of the cases calculated in the present calculation are summarized in Table 2.

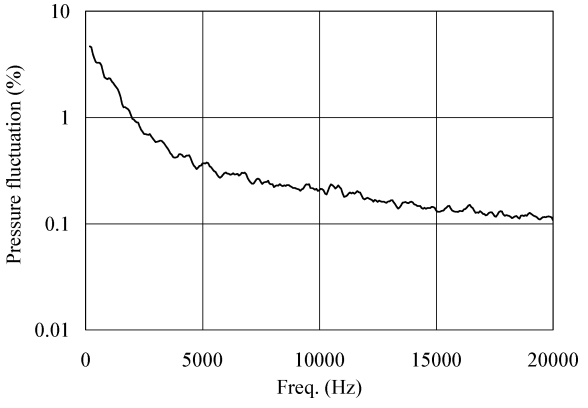

Fig. 3 Power spectrum of the pressure fluctuation in the JAXA 2×2 m transonic wind tunnel measured by Oguni et al.[14]

Table 1 Summary of flow conditions in the present experiment

Test case no.	Test conditions		
	M	P_0, kPa	T_0, K
1	1.20 ± 0.01	50.0 ± 0.5	310.5 ± 1.2
2	1.20 ± 0.01	52.0 ± 0.4	311.2 ± 0.7
3	1.20 ± 0.01	54.0 ± 0.3	310.0 ± 0.9
4	1.20 ± 0.01	55.0 ± 0.3	310.1 ± 0.9
5	1.20 ± 0.01	57.1 ± 0.5	311.6 ± 0.8
6	1.20 ± 0.01	58.0 ± 0.4	310.3 ± 0.8
7	1.20 ± 0.01	60.0 ± 0.4	312.0 ± 0.8
8	1.20 ± 0.01	63.0 ± 0.4	311.8 ± 0.8
9	1.20 ± 0.01	65.0 ± 0.4	312.0 ± 0.8
10	1.20 ± 0.01	67.0 ± 0.4	312.0 ± 0.7
11	1.20 ± 0.01	70.0 ± 0.4	309.4 ± 0.7
12	1.20 ± 0.01	70.0 ± 0.4	310.5 ± 0.7
13	1.20 ± 0.01	70.0 ± 0.4	311.7 ± 0.7
14	1.20 ± 0.01	80.0 ± 0.6	313.1 ± 1.2
15	1.20 ± 0.01	90.1 ± 0.7	314.5 ± 0.8

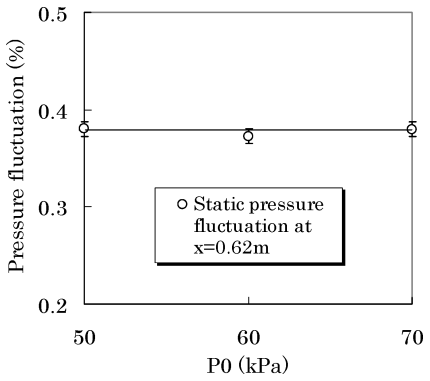

Fig. 4a Effect of total pressure on static-pressure fluctuation on the model.

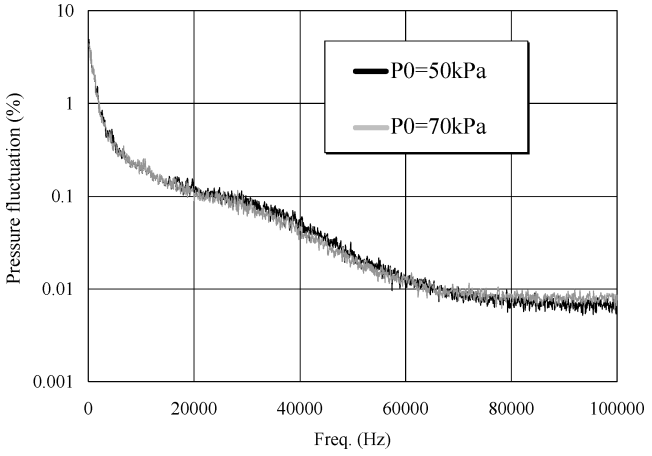

Fig. 4b Effect of total pressure on the power spectrum of the static-pressure fluctuation.

Measurement Technique

Infrared Camera

A 12-bit IR camera[15] was used to map the transition front with little influence of surface roughness. To acquire full surface distribution of the transition front, the camera was placed in two different positions as shown in Fig. 5, and IR images were taken from three sides. The bottom view of the model at a positive incidence was taken by setting negative incidence of the same magnitude.

Because the camera was placed inside the plenum chamber where the static pressure is 20.6 kPa at $M = 1.2$, it was installed in an atmospheric pressure chamber.

IR camera technique is based on measurements detecting variable wall temperatures in the transition region as a result of different recovery temperatures of laminar and turbulent flows.

Table 2 Flow conditions in the present calculation

Calculation case no.	M	AOA, deg	P_0, kPa	T_0, K	Corresponding test case no. in Table 1
I	1.2	2	54	310.0	3
II	1.2	1	55	310.6	4
III	1.2	0, 1, 2, 3, 4	70	311.2	13
IV	1.2	0	90	314.5	14

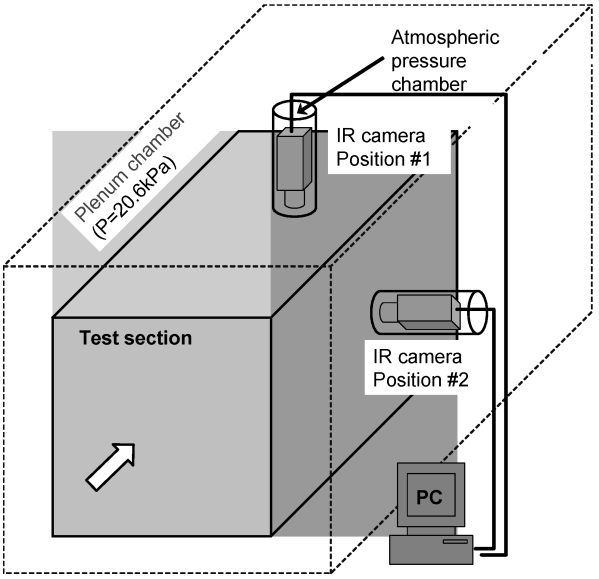

Fig. 5 Infrared camera setup.

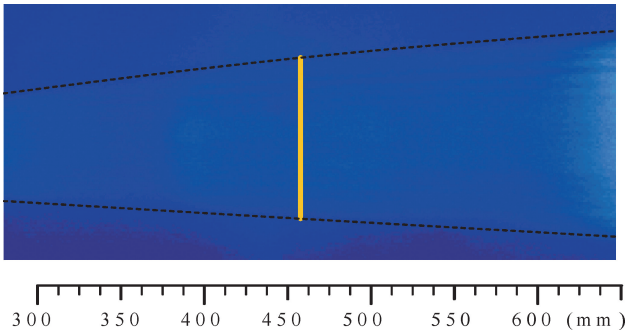

Fig. 6a Side view of surface-temperature distribution at 0-deg AOA and $P_0 = 50$ kPa (test case 1).

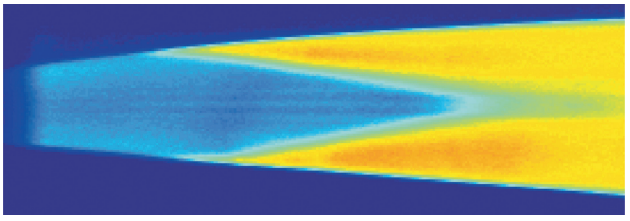

Fig. 6b Top view of surface-temperature distribution at 2-deg AOA and $P_0 = 70$ kPa (test case 12).

Figure 6a shows a raw IR image acquired at 0-deg AOA (test case 1). The circumferential temperature distribution of its profile is shown in Fig. 7 (test case 1). The position of the profile is shown as a straight line in Fig. 6a. Here, ϕ is defined as a cone meridian angle measured from the intersection line of the model surface and the plane defined by the center axis of the model and the focal point of the camera. Figure 7 shows that the IR signal is constant with a scatter within ±0.1 K in the range of $|\phi| < 82$ deg and degrades in the peripheral area. A measurement of optic-angle dependency of the temperature measured using this camera[15] was carried out

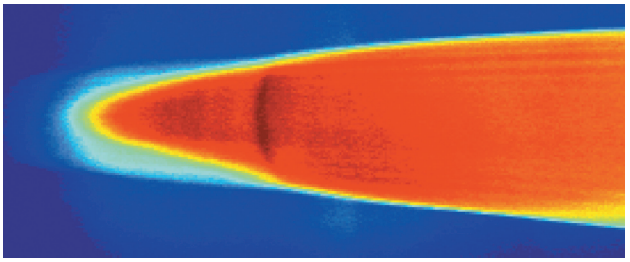

Fig. 6c Side view of surface-temperature distribution at 2-deg AOA and $P_0 = 70$ kPa (test case 13).

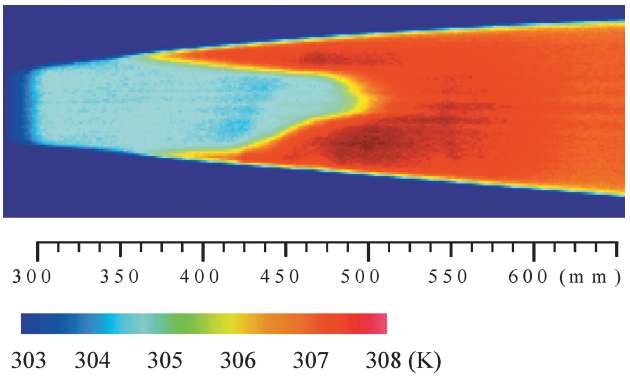

Fig. 6d Bottom view of surface-temperature distribution at 2-deg AOA and $P_0 = 70$ kPa (test case 13).

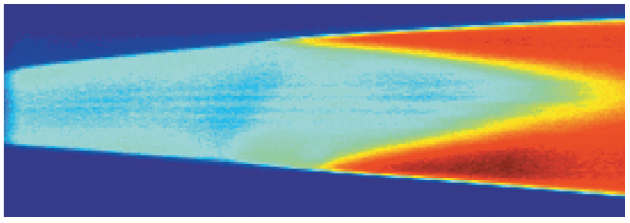

Fig. 6e Top view of surface-temperature distribution at 1-deg AOA and $P_0 = 70$ kPa (test case 13).

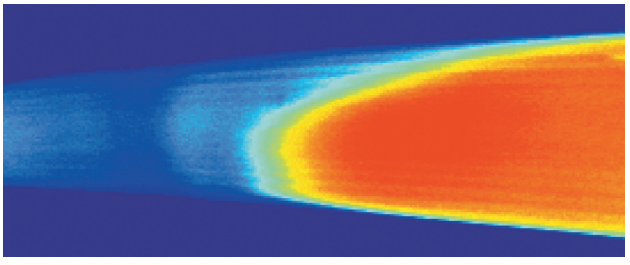

Fig. 6f Side view of surface-temperature distribution at 1-deg AOA and $P_0 = 70$ kPa (test case 13).

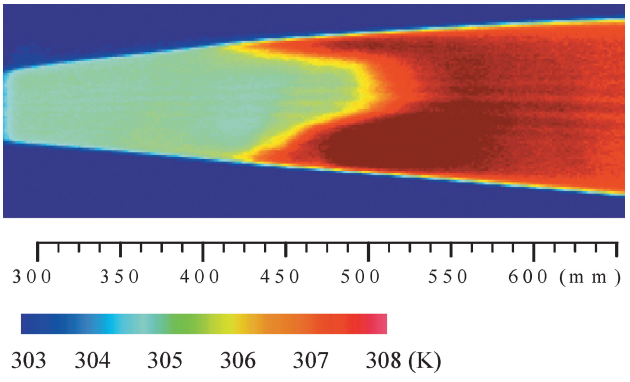

Fig. 6g Bottom view of surface-temperature distribution at 1-deg AOA and $P_0 = 70$ kPa (test case 13).

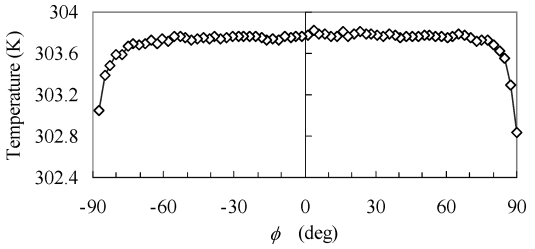

Fig. 7 Circumferential distribution of surface tempertature at 0-deg AOA (test case 1).

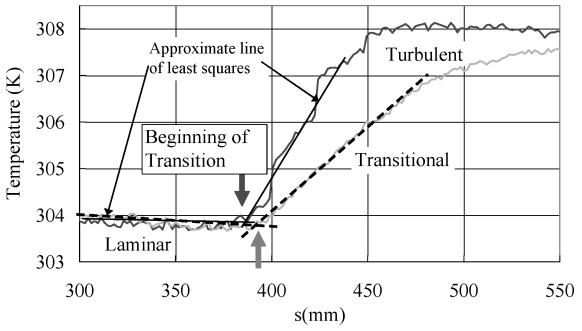

Fig. 8 Examples of temperature profiles along two streamlines measured using IR camera (test case 11). The dark gray line shows a temperature profile along a streamline that rans through a point $x = 400$ mm and $\theta = 39$ deg, and the light gray line shows one along a streamline that runs through a point $x = 400$ mm and $\theta = -39$ deg.

for a variable-angle flat plate whose temperature is kept constant using a thermostat. The measurement showed that the measured temperatures at 70- and 75-deg optic angle were 95 and 93% of those at 0-deg optic angle, respectively. Thus, every data analysis was made in the range of $|\phi| < 75$ deg.

Distortion and aeroelastic deformation were corrected by three-dimensional affine transformation. The actual coordinates of the model were measured at no-wind condition by putting markers made of aluminum tape on the model surface.

Figure 8 shows two typical temperature profiles along the streamlines (test case 11). The dark gray line shows a temperature profile along a streamline that run through a point at $x = 400$ mm and $\theta = 39$ deg, and the light gray line shows one along a streamline that runs through a point $x = 400$ mm and $\theta = -39$ deg. The coordinates of the streamlines were calculated using a three-dimensional Navier–Stokes (N-S) code. This code uses the Baldwin–Lomax model and was previously validated by experiments and other numerical codes.[16] The temperature remains constant when the flow is either laminar or turbulent and changes linearly with distance during the transition. Thus, the beginning of the transition was defined as the location of the intersection point of two approximate lines of least squares respectively through the laminar and turbulent region. The temperatures at the beginnings of transition along both streamlines coincide. This shows that transition front coincides with an isotemperature line (in this case, $T = 304.0$ K).

The accuracy of the location of the beginning of transition obtained using the IR camera is estimated to be 1%. The estimation is based on the image length of 1.2 mm corresponding to one pixel and temperature resolution of 0.08 K. Temperature resolution of the infrared camera is 0.08 K, which is very small compared to our observed differences between surface temperature of laminar and turbulent boundary layer that were in the 3–4-K range.

Unsteady Pressure Transducer

The unsteady pressure transducer (Kulite XCQ062) was also used to investigate the nature of the disturbance present at the initial stage of transition.

The propriety of the use of an unsteady pressure transducer for the disturbance measurement must be considered. From the

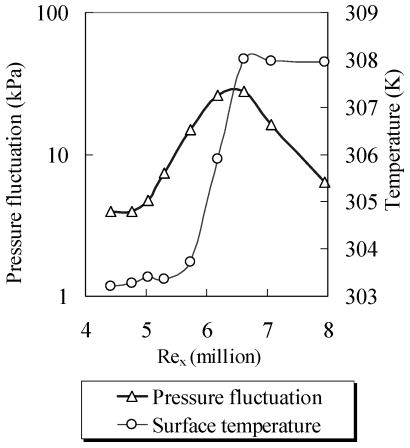

Fig. 9 Comparison between surface temperature and pressure fluctuation at $x = 620$ mm on the windward ray ($\theta = 180$ deg).

one-dimensional isentropic relations,

$$p + \rho u^2 = \text{const} \tag{2}$$

where p, ρ, and u stand for static pressure, density, and velocity of the flow, respectively. Writing each quantity as the instantaneous deviations of a fluctuating quantity with reference to its temporal mean value gives

$$p = \bar{p} + p', \qquad u = \bar{u} + u', \qquad \rho u = \overline{\rho u} + (\rho u)' \tag{3}$$

Equation (2) is then equivalent to

$$p'/\bar{p} = \gamma M^2[(\rho u)'/\overline{\rho u} + u'/\bar{u}] \tag{4}$$

Hence, pressure fluctuation is proportional to a sum of mass-flow fluctuation and velocity fluctuation.

The pressure fluctuation was measured with bandwidth from 125 Hz to 100 kHz.

Correlation of data against a unit Reynolds number using the IR camera and the unsteady pressure transducer is given in Fig. 9. The location of the pressure fluctuation and surface-temperature data is fixed at $x = 620$ mm station, and the total pressure of the flow is varied. The pressure fluctuation data clearly show a rise from the laminar to turbulent level with an intermediate peak. The rise in the fluctuation data takes place at a lower Reynolds number than for the beginning of transition defined by the surface temperature. This is apparently because a change in a fluctuating quantity occurs earlier than a change in a mean-flow quantity such as surface temperature. Note that location of peak fluctuation coincides with the maximum surface-temperature location. It has been established by Owen[17] that the location of peak voltage fluctuation determined using hot-film sensors on a surface coincides with the maximum burst frequency location and the maximum surface-temperature location. Accordingly, the peak location of the pressure and the hot-film voltage fluctuation coincide; this proves the consistency of the present stability measurement by the pressure transducer.

The intermittency factor was calculated from the pressure fluctuation data by the method proposed by Townsend.[18] Kurtosis is calculated from measurements of the flattening factors, assuming that the flattening factors taken only during periods of turbulent flow are identical with those observed in fully turbulent flow, where experiment in isotropic turbulence has shown that

$$\frac{\overline{u^4}}{(\overline{u^2})^2} = \frac{\overline{v^4}}{(\overline{v^2})^2} = \frac{\overline{w^4}}{(\overline{w^2})^2} = 3.00 \tag{5}$$

where u, v, and w stand for streamwise, spanwise, and vertical components of the flow velocity, respectively. Then, intermittency factor is

$$\gamma = 3.0\frac{(\overline{u^2})^2}{\overline{u^4}} = 3.0\frac{(\overline{v^2})^2}{\overline{v^4}} = 3.0\frac{(\overline{w^2})^2}{\overline{w^4}} \tag{6}$$

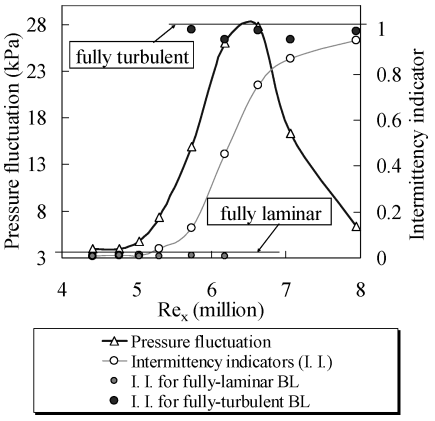

Fig. 10 Comparison between intermittency and magnitude of surface-pressure fluctuation at $x = 620$ mm on the windward ray ($\theta = 180$ deg).

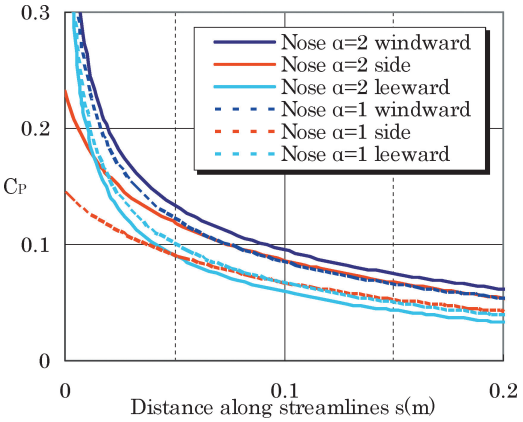

Fig. 11 Calculated pressure distributions at 1- and 2-deg AOA (calculation case III).

Based on Eq. (4), we assume that the following relation can be used for the pressure fluctuation:

$$\gamma = 3.0\frac{(\overline{p^2})^2}{\overline{p^4}} \tag{7}$$

The assumption is justified by the consistency of values of γ measured in this way (Fig. 10).

The accuracy of the pressure fluctuation is estimated to be 2%. The estimation is based on the diameter of the transducer, 1.6 mm, resolution of 0.1%, and an assumed estimation error of 1.5% in the process of static-pressure calibration.

Results and Discussion

Surface-Pressure Distributions

Calculated pressure distributions along streamlines on the model at 1- and 2-deg AOA are shown in Fig. 11 (calculation case III). Each pressure distribution was validated by the measured pressure using static ports fixed at $x = 400$-, 500-, and 550 mm station. The pressure transducer fixed at $x = 620$ mm lies on the streamline labeled "side" in the figures, when the transducer is set at $\theta = 90$ deg. Here, θ is defined as a cone meridian angle measured from the leeward ray. The streamlines and the calculated pressure distributions were obtained with the same three-dimensional N-S code used in the preceding section. The agreement between the measurements and the computation is very good. Large favorable pressure gradients exist along the streamlines on the model at every AOA. Note that at each AOA the smallest maximum pressure gradient is achieved on the windward ray and that the gradient on the leeward ray is greater.

Distributions of Transition Fronts

Figures 6b, 6c, and 6d show top, side, and bottom views of surface-temperature distribution of the model at 2-deg AOA and

$P_0 = 70$ kPa, respectively, determined using the IR camera (test cases 12, 13, and 13 respectively). Figures 6e, 6f, and 6g show the top, side, and bottom views at 1-deg AOA and $P_0 = 70$ kPa, respectively (test case 13). The transition front coincides with $T = 305.0$ K line in Fig. 6b and $T = 306.0$ K lines in the rest of the figures. The difference in the temperatures of transition front comes from the fact that total temperature temporarily dropped to a 1-K lower value of 310.5 K (test case 12) when the distribution of Fig. 6b was acquired and the rest of the figures were acquired at temperatures in the range from 311.2 to 312.1 K (test case 13). [The lower temperature at the beginning of transition in Fig. 8 is also explained by the drop of total temperature to 309.4 K (test case 11).] The foremost transition occurred at $\theta = 90$ deg at each AOA. The transition occurred more aft on the leeward ray than on the windward ray at each AOA; the most aft transition occurred on the leeward ray.

Overall, the shapes of the transition front are similar at both AOA. However, note that the shapes of the transition front near the leeward ray are different; an angle determined by the transition front is acute at 2-deg AOA but is obtuse at 1-deg AOA.

The previous studies on the cones have consistently found that the transition front moves monotonically forward between the windward ($\theta = 180$ deg) and the leeward ray ($\theta = 0$ deg) (Refs. 3–6). As on the cones, in the range from $\theta = 90$ to 180 deg, the measurements show the transition point moving rearward with increasing θ. A unique feature of the present model is that the most aft transition occurred on the leeward rays ($\theta = 0$ deg) rather than on the windward rays ($\theta = 180$ deg) as observed on the cones.

As already stated, the maximum pressure gradient was smaller on the windward ray ($\theta = 180$ deg) than on the leeward ray ($\theta = 0$ deg) at each AOA; this might account for the more aft transition point on the leeward ray rather than on the windward ray. However, because different instability mechanisms might be responsible for transition on both rays, this will be discussed further in the following section.

The smallest maximum pressure gradient along the streamlines was achieved on the windward ray ($\theta = 180$ deg). Accordingly, from $\theta = 50$ to 150 deg, the transition occurred more forward from $\theta = 50$ to 150 deg than $\theta = 180$ deg despite the larger pressure gradient along the streamlines. Because the favorable pressure gradient amplifies C-F instabilities but stabilizes T-S instabilities, this implies that C-F instability dominates the transition. However, additional measurements are needed for justification. Because the foremost transition occurred at $\theta = 90$ deg, let us concentrate our attention on this angle.

Thus, to identify instability mechanisms at $\theta = 90$ deg and on the windward ($\theta = 180$ deg) and leeward rays ($\theta = 0$ deg), additional measurements were carried out using the unsteady pressure transducer.

Boundary-Layer Disturbance Spectra

Figure 12a shows the effect of total pressure on power spectrum at a point at $x = 620$ mm at 0-deg AOA (test cases 1, 14, and 15). Significant disturbance growth is clearly observed in the 10–20-kHz

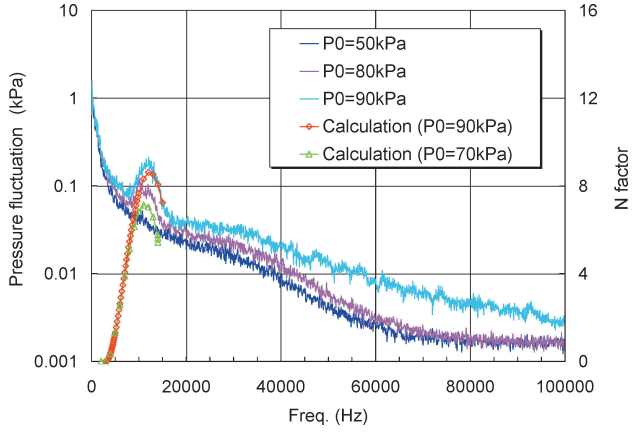

Fig. 12a Power spectrum at $x = 620$ mm at 0-deg AOA (test cases 1, 14, and 15; calculation cases III and IV).

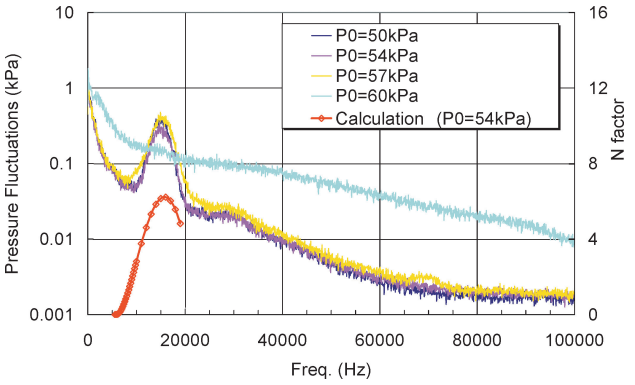

Fig. 12b Power spectrum at $x = 620$ mm on the windward ray ($\theta = 180$ deg) at 2-deg AOA (test cases 1, 3, 5, and 7; calculation case I).

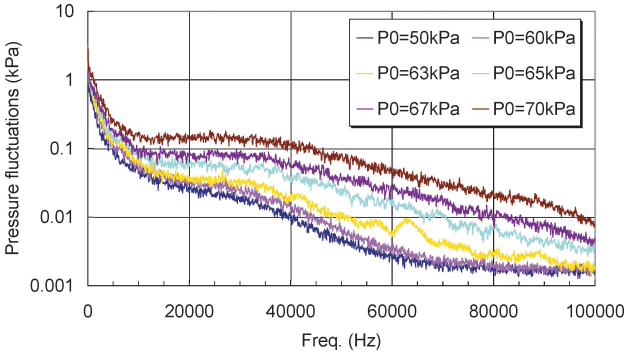

Fig. 12c Power spectrum at $x = 620$ mm on the leeward ray ($\theta = 0$ deg) at 2-deg AOA (test cases 1, 7–10, and 13).

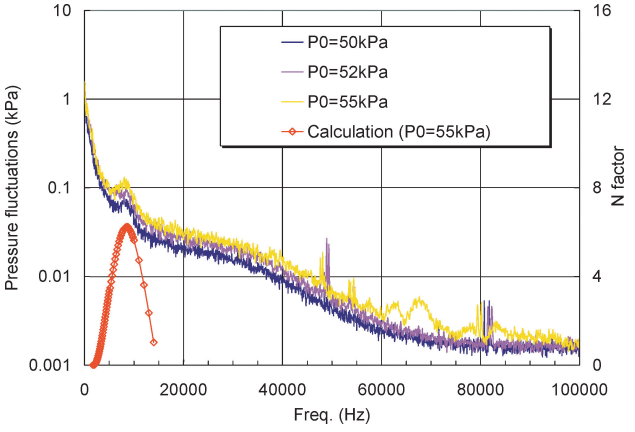

Fig. 12d Power spectrum at $x = 620$ mm on the leeward ray ($\theta = 0$ deg) at 1-deg AOA (test cases 1, 2, and 4; calculation case II).

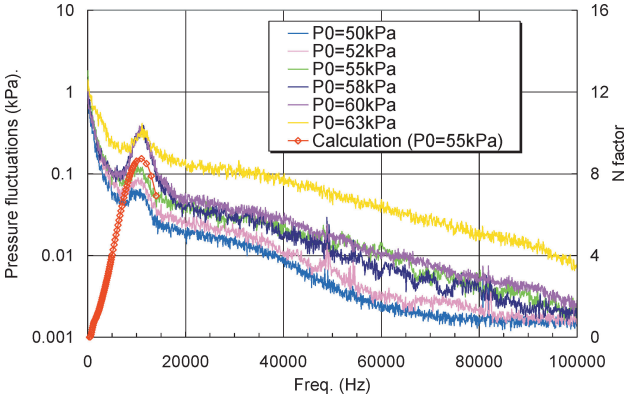

Fig. 12e Power spectrum at $x = 620$ mm and $\theta = 90$ deg at 1-deg AOA (test cases 1, 2, 4, and 6–8; calculation case II).

frequency band, with peak amplitude at 12 kHz. The maximum amplified frequency calculated at $P_0 = 90$ kPa using a compressible e^N code with an envelope method strategy is also plotted in the figure (calculation case IV). In the calculation, compressible laminar boundary-layer profiles were calculated using a three-dimensional N-S code with 70 grid points in the boundary layer. The profiles were validated using an axisymmetric laminar boundary-layer code[10] based on the methods developed by Kaups and Cebeci. Nonparallel and curvature effects are not included in the present code. The e^N code is validated experimentally and using another linear stability code[19] developed by Arnal et al. based on the envelope method. Disturbance growth by the effect of total pressure is also clear in the calculated N-value curve. The calculated maximum amplified frequency increased by 1 kHz from $P_0 = 70$ to 90 kPa; this is likely to be associated with a decrease in the wavelength of the disturbance caused by a decrease in boundary-layer thickness. However, the existence of the shift in the experimental power spectrums is not clear in the figure. The calculated frequency and the measured peak frequency at $P_0 = 90$ kPa are in very good agreement.

Figure 12b shows the effect of total pressure on power spectrum at $x = 620$ mm on the windward ray ($\theta = 180$ deg) at 2-deg AOA (test cases 1, 3, 5, and 7), together with a calculated maximum-amplified frequency at $P_0 = 54$ kPa (calculation case I). Significant disturbance growth is clearly observed in the 10–20-kHz frequency band, with peak amplitude at 16 kHz. The calculated frequency and the measured peak frequency are in good agreement. Because of symmetry of the flow, crossflow velocity components are zero along the windward ray. Therefore, we can be fairly certain that T-S instability dominates the transition. As for the cones, T-S instability also dominates on the leeward ray according to the stability measurements.[7–8] Hence, the stability mechanism on the leeward ray does not change in the presence of the large pressure gradient.

Figure 12c shows the effect of total pressure on power spectrum at $x = 620$ mm on the leeward ray ($\theta = 0$ deg) at 2-deg AOA (test cases 1, 7–10, and 13). Note that fluctuations of all frequencies grow monotonically and that there is clearly no frequency dependency despite measurement with minute 2–3-kPa steps in total pressure.

Figure 12c shows that the spectrum at $P_0 = 50$ kPa coincides with that on the windward ray ($\theta = 180$ deg) at $P_0 = 50$ kPa shown in Fig. 12a, which is apparently laminar. This suggests that the boundary layer is laminar on the leeward ray at $P_0 = 50$ kPa.

Figure 13 shows the effect of total pressure on the magnitude of the pressure fluctuation (test cases 1, 3, 5, 7–10, and 13). Intermittency factors are also plotted in the figure. There is a clear relationship between the magnitude of the pressure fluctuation and the intermittency factor of the signal. This relationship suggests that the rise in the pressure fluctuation is caused by an increase in the intermittency of the flow. Figure 14 shows the time-coordinate output signals of the unsteady pressure transducer (test cases 1 and 10). A burst-like signal is observed at total pressures above 64 kPa.

The angle between the transition front and each streamline is 9 deg, which lies in the range of 8–11 deg of half-apex angle of turbulent wedge.[20] All of these things make it clear that the acute angle of the transition front was determined by turbulent wedges formed as a consequence of the more foreword transition on the side.

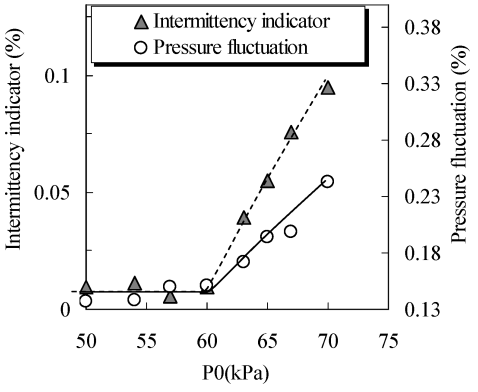

Fig. 13 Comparison between intermittency and magnitude of pressure fluctuation at $x = 620$ mm on the leeward ray ($\theta = 0$ deg) at 2-deg AOA (test cases 1, 3, 5, 7–10, and 13).

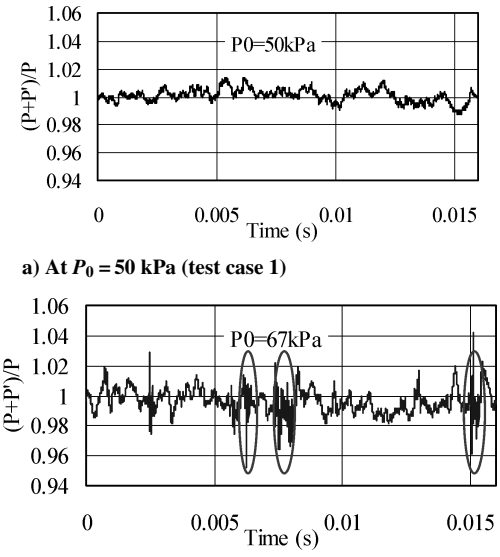

Fig. 14 Pressure fluctuation at $x = 620$ mm on the leeward ray ($\theta = 0$ deg).

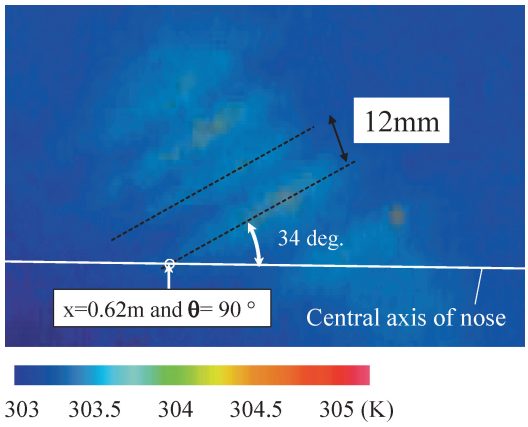

Fig. 15 Enlarged view of surface-temperature distribution near $x = 620$ mm and $\theta = 90$ deg (test case 4).

Figure 12d shows the effect of total pressure on power spectrum at $x = 620$ mm on the leeward ray ($\theta = 0$ deg) at 1-deg AOA (test cases 1, 2, and 4). The calculated frequency at $P_0 = 55$ kPa (calculation case II) and the measured peak frequency are in good agreement. Therefore, the disturbance is assumed to be T-S wave. Thus, the difference of the angles of the transition front near the leeward ray can be attributed to whether the transition on the side occurs sufficiently forward. Accordingly, it is likely that at 2-deg AOA, without the influence of the transition on the side, the transition is dominated by T-S instability, and the transition point moves further rearward. As for the cones, flow profiles along the leeward ray are highly inflectional according to the profile measurements.[7,8] Hence, in the presence of the large pressure gradient the inflectional profile does not seem to exist on the leeward rays.

Because at 2-deg AOA the flow is turbulent at $x = 620$ mm and $\theta = 90$ deg even at the least attainable Reynolds number, let us concentrate our attention on the measurement at 1-deg AOA. Figure 15 shows an enlarged view of surface-temperature distribution around $x = 620$ mm and $\theta = 90$ deg at 1-deg AOA (test case 4). Stationary crossflow vortices are evident in the figure as light-dark patterns. The difference between the light and dark patterns is 0.7 K, and the spacing of the vortices is 12 mm. The calculated wavelength of the crossflow wave is 12.1 mm (calculation case II) and is in very good agreement with the measured spacing. The inclination

angle between vortices and the central axis is 34 ± 3 deg and is in fairly good agreement with a 38-deg angle between the calculated propagation direction of the maximum amplified disturbance and the central axis. The ±3-deg band shows 95% coverage of the inclination angle and is relatively large because the figure was enlarged from a relatively small area of the original IR image. The 4-deg difference could be caused by a nonlinearity or a failure of the envelope method in capturing the developmental history of the disturbance. As already stated, the transition occurred more forward than on the windward ray in the presence of the larger pressure gradient, which amplifies C-F instabilities but stabilizes T-S instabilities. From these observations, it is assumed that C-F instability dominates the transition at $\theta = 90$ deg. As for the cones, crossflow instabilities dominate on the side according to the several observations of streamwise vortices.[3,9,10] Hence, in the presence of the large pressure gradient the stability mechanism on the side does not change but affects the transition near the leeward ray.

Figure 12e shows the power spectrum at $x = 620$ mm and $\theta = 90$ deg at 1-deg AOA (test cases 1, 2, 4, and 6–8). Disturbance growth is clearly observed in the 6–15-kHz frequency band, with peak amplitude at 11 kHz. Note that the amplitude is smaller than on the windward rays. The calculated frequency at $P_0 = 55$ kPa (calculation case II) and the measured peak frequency are in good agreement. However, the agreement is open to question because the envelope method assumes that a crossflow wave can suddenly change to a streamwise wave. The calculated frequency of the T-S wave on the windward and leeward ray are 14 and 8.4 kHz, respectively, and both frequencies are different from this value. Thus, the observed disturbance does not originate in either ray. Several observations in the last few paragraphs imply that the disturbance is C-F traveling wave mode. Measurement by Bippes et al.[21] indicated that traveling wave rather than stationary mode is dominant in high-turbulence environment of the order of $Tu = 0.30\%$ and vice versa in low-turbulence environment ($Tu = 0.05\%$). Hence, the traveling wave seems to be observed because of the high-turbulence environment ($C_{P\mathrm{rms}} = 0.34\%$).

Conclusions

Boundary-layer transition on the forward part of a Sears–Haack body at 1- and 2-deg incidence was investigated at Mach 1.2. Surface roughness was 0.22-μm rms. The static-pressure fluctuation normalized by dynamic pressure $C_{P\mathrm{rms}}$ was 0.34%, and the spectral content of the pressure fluctuation was fully documented.

Tollmien–Schlichting instability dominated the transition process on the windward ray ($\theta = 180$ deg) similar to the transition on sharp cones.

The most aft transition at each AOA occurred on the leeward ray ($\theta = 0$ deg) rather than on the windward rays ($\theta = 180$ deg) as observed on the sharp cones. Inflectional profile does not seem to exist on the leeward rays ($\theta = 0$ deg), which was different from the sharp cones. At 2-deg AOA, the transition front near the leeward ray ($\theta = 0$ deg) was determined by turbulent wedges formed as a consequence of the more forward transition on the side.

The foremost transition occurred at $\theta = 90$ deg. Crossflow instability was assumed to dominate on the side similar to the transition on the cones. Stationary crossflow vortices were evident in the surface-temperature distribution obtained with IR camera. The disturbance believed to be a traveling crossflow wave was observed at 1-deg incidence. This seemed to be caused by the high-turbulence environment.

Acknowledgments

The authors acknowledge the help and advice received from Akira Nishizawa and Kenji Yoshida of the Japan Aerospace Exploration Agency. We also thank Tadao Koyama, who developed the whole infrared camera system used in this research, and Koji Izumi and Shohei Takagi of JAXA for their advice and encouragement.

References

[1]Ueda, Y., and Yoshida, K., "Numerical Study on Optimum Pressure Distribution for Supersonic Natural Laminar Flow Design," *Proceedings of the 32nd Fluid Dynamics Conference*, Vol. 32, Japan Society for Aeronautical and Space Sciences, Tokyo, 2000, pp. 271–274 (in Japanese).

[2]Schmisseur, J. D., Schneider, S. P., and Collicott, S. H., "Receptivity of the Mach-4 Boundary-Layer on an Elliptic Cone to Laser-Generated Localized Freestream Perturbations," AIAA Paper 98-0532, Jan. 1998.

[3]King, R. A., "Three-Dimensional Boundary-Layer Transition on a Cone at Mach 3.5," *Experiment in Fluids*, Vol. 13, No. 5, 1992, pp. 305–314.

[4]Stetson, K. F., "Mach 6 Experiments of Transition on a Cone at Angles of Attack," *Journal of Spacecraft and Rockets*, Vol. 19, No. 5, 1982, pp. 397–403.

[5]Krogmann, P., "An Experimental Study of Boundary Layer Transition on a Slender Cone at Mach 5," AGARD CP 224, May 1977.

[6]Reda, D. C., "Boundary Layer Transition Experiments on Sharp, Slender Cone at Mach 5," AIAA Paper 78-1129, 1978.

[7]Doggett, G. P., Chokani, N., and Wilkinson, S. P., "Effect of Angle of Attack on Hypersonic Boundary-Layer Stability," *AIAA Journal*, Vol. 35, No. 3, 1997, pp. 464–470.

[8]Ladoon, D. W., and Schneider, S. P., "Measurements of Controlled Wave Packets at Mach 4 on a Cone at Angle of Attack," AIAA Paper 98-0436, Jan. 1998.

[9]Ivanov, A. R., "The Effect of the Bluntness and the Half-Angles of a Cone on the Turbulent Transition of a Boundary-Layer at Free-Stream Mach 6," *Uchenye Zapiski*, Vol. 15, No. 3, 1984, pp. 132–135 (in Russian).

[10]McDevitt, J. B., and Mellenthin, J. A., "Upwash Patterns on Ablating and Nonablating Cones at Hypersonic Speeds," NASA TN D-5346, July 1969.

[11]Meier, H. U., and Kreplin, H., "Experimental Investigation of the Boundary Layer Transition and Separation on a Body of Revolution," *Zeitschrift für Flugwissenschaften und Weltraum-Forschung*, Vol. 4, No. 2, 1980, pp. 65–71.

[12]Spall, R. E., and Malik, M. R., "Linear Stability of Three-Dimensional Boundary Layers over Axisymmetric Bodies at Incidence," *AIAA Journal*, Vol. 30, No. 4, 1992, pp. 905–913.

[13]Radeztsky, R. H., Reibert, M. S., and Saric, W. S., "Effect of Isolated Micron-Sized Roughness on Transition in Swept-Wing Flows," *AIAA Journal*, Vol. 37, No. 11, 1999, pp. 1370–1377.

[14]Oguni, Y., Nakamura, S., Hosoe, N., and Kawamoto, I., "The Evaluation of Flow Characteristics of 2m × 2m Transonic Wind Tunnel," *Proceedings of the 94th Meeting of Supersonic Tunnel Association, International*, Vol. 94, Aeronautical Research Inst. of Sweden, Bromma, Sweden, 2000, pp. 1–10.

[15]Koyama, T., and Tsuda, S., "Measurement of Heat Transfer Distribution by Infrared Thermography Technology," *Journal of the Visualization Society of Japan*, Vol. 19, No. 75, 1999, pp. 267–272.

[16]Takaki, R., Iwamiya, T., and Aoki, A., "CFD Analysis Applied to the Supersonic Research Airplane," *Proceedings of the 1st International CFD Workshop for Supersonic Transport Design*, Vol. 1, Japan Aerospace Exploration Agency, Tokyo, 1998, pp. 68–72.

[17]Owen, F. K., "Transition Experiments on a Flat Plate at Subsonic and Supersonic Speeds," *AIAA Journal*, Vol. 8, No. 3, 1970, pp. 518–523.

[18]Townsend, A. A., "Momentum and Energy Diffusion in the Turbulent Wake of a Cylinder," *Proceedings of the Royal Society of London, Series A*, Vol. 197, No. A1048, 1949, pp. 124–140.

[19]Yoshida, K., Ueda, Y., Sugiura, H., Tokugawa, N., Atobe, T., Arnal, D., Archamboud, J. P., and Seraudie, A., "Boundary Layer Transition Analysis on NEXST-1 Airplane: NAL-ONERA Cooperative Research Project," *Proceedings of the 3rd International Workshop on Supersonic Civil Aircraft*, Vol 3, Japan Aerospace Exploration Agency, Tokyo, 2001, pp. 1–6.

[20]Charters, A. C., "Transition between Laminar and Turbulent Flow by Transverse Contamination," NACA TN-891, March 1943.

[21]Bippes, H., Muller, B., and Wagner, M., "Measurements and Stability Calculations of the Disturbance Growth in an Unstable Three-Dimensional Boundary Layer," *Physics of Fluids A*, Vol. 3, No. 10, 1991, pp. 2371–2377.

H. Reed
Associate Editor

Color reproductions courtesy of the Japan Aerospace Exploration Agency.